


Topological Mott transition in a Weyl-Hubbard model: Dynamical mean-field theory studyBernhard Irsigler^{1,2}, Tobias Grass,² Jun-Hui Zheng,³ Mathieu Barbier,¹ and Walter Hofstetter¹¹*Institut für Theoretische Physik, Goethe-Universität, 60438 Frankfurt am Main, Germany*²*ICFO-Institut de Ciències Fòniques, The Barcelona Institute of Science and Technology, 08860 Castelldefels (Barcelona), Spain*³*Center for Quantum Spintronics, Department of Physics, Norwegian University of Science and Technology, NO-7491 Trondheim, Norway* (Received 19 November 2020; revised 18 February 2021; accepted 4 March 2021; published 15 March 2021)

Weyl semimetals are three-dimensional, topologically protected, gapless phases which show exotic phenomena such as Fermi arc surface states or negative magnetoresistance. It is an open question whether interparticle interactions can turn the topological semimetal into a topologically nontrivial Mott-insulating phase. We investigate an experimentally motivated model for Weyl physics of cold atoms in optical lattices, with the main focus on interaction effects and topological properties, by means of dynamical mean-field theory. We characterize topological phases by numerically evaluating the Chern number via the Ishikawa-Matsuyama formula for interacting phases. Within our studies, we find that the Chern numbers become trivial when interactions lead to insulating behavior. For a deeper understanding of the Weyl-semimetal-to-Mott-insulator topological phase transition, we evaluate the topological properties of quasiparticle bands as well as so-called blind bands. Finally, we consider a system with an open boundary along one spatial direction in order to study correlation effects of surface states. In a narrow regime close to the topological phase transition, we find a correlation-induced state in which the surface becomes metallic while the bulk is semimetallic.

DOI: [10.1103/PhysRevB.103.125132](https://doi.org/10.1103/PhysRevB.103.125132)**I. INTRODUCTION**

Topological states of matter realized with cold atoms in optical lattices are a vibrant field at the forefront of modern quantum research [1–5]. The great control and tunability of cold atoms in optical lattices make them an ideal analog quantum simulator of tight-binding Hamiltonians [6,7]. Among pioneering experiments in the context of topological states are the realizations of two prominent theoretical two-dimensional (2D) models: the Hofstadter [8] and the Haldane [9] models. The former is realized by imprinting a complex quantum phase onto the particles upon hopping in the lattice through laser-assisted tunneling [10,11]. The latter is engineered through elliptic lattice shaking which also imprints a complex phase according to Floquet's theorem [12,13]. Both approaches are well described by effective static Floquet Hamiltonians with gauge fields as a result of high-frequency driving [14,15].

The current focus of research in this field clearly lies in 2D systems. One reason is the fact that 2D systems host paradigmatic phases such as the quantum Hall effect. The possible existence of topological phases is connected to the dimensionality and symmetries of the system of interest [16]. In contrast to 2D, in three-dimensional (3D) systems, even gapless states can be topologically protected. Examples are the Weyl semimetal (WSM) and nodal-line semimetals [17,18].

Moreover, the search for an exotic topological Mott insulator is still a hot topic [19]. Topological Mott insulators are still not well understood. The idea is that strong interactions cause the particles to undergo a Mott transition such that charge degrees of freedom are gapped out. Spin degrees of freedom,

on the other hand, might still show topological properties such as the bulk-boundary correspondence. Being a highly correlated state due to the Mott gap, topologically nontrivial Mott insulators are not adiabatically connected to a noninteracting state. In contrast to a topologically trivial Mott insulator, a topologically nontrivial Mott insulator should exhibit some nonzero topological invariant. The original work suggested a topological Mott insulator in 3D [20]. However, studies of 1D [21] and 2D [22,23] topological Mott insulators exist as well. Also, topological Mott insulators incorporating long-range interactions through Rydberg atoms have also been investigated [24,25].

WSMs host gapless Weyl points (WPs) in the 3D Brillouin zone (BZ) which are topologically protected, i.e., they cannot gap out through smooth deformations of the Hamiltonian. One generally differentiates between WSMs with broken time-reversal symmetry or WSMs with broken inversion symmetry [18]. If both are broken, the WPs are not located at the Fermi level [26]. WSMs have first been observed in 2015 in a TaAs crystal along with the exotic Fermi arc surface states by means of photoemission spectroscopy [27] as well as in a gyroid photonic crystal [28], both with broken inversion symmetry. Another intriguing feature of WSMs is the chiral anomaly and the resulting negative magnetoresistance which was also measured in TaAs crystals [29]. Recently, a nodal-line semimetal has been engineered as the first instance of a 3D topological state in a cold-atom setup [30], but the realization of an atomic WSM is still lacking.

In the interacting case, the Weyl-Mott insulator has been proposed as an extension to the noninteracting WSM [31]. The model has a momentum-locked interaction and is

analytically solvable. This is possible through the assumption of this particular form of the interaction. Moreover, the system has a Mott gap as well as a nontrivial topological invariant in terms of the single-particle Green's function. Reference [32] pointed out that this invariant does not imply the presence of a single-particle Fermi arc because of the absence of the WPs in the single-particle spectrum. Instead, the system has gapless particle-hole pair excitations, suggesting the existence of the Weyl points in the bosonic excitation spectrum. The nonzero topological invariant indeed implies the presence of a bosonic surface state. While a single-particle Fermi arc is observable through photoemission spectroscopy [27], the bosonic surface is not accessible with photoemission spectroscopy.

In Ref. [31], the interactions which give rise to the Weyl-Mott insulator are local in momentum space, whereas in realistic systems, the interactions are rather local in real space. In this paper, we investigate the effect of realistic onsite interactions on a WSM. To analyze the topological properties of such a system, we compute the topological invariants in terms of the single-particle Green's function. In most cases, this quantity is well suited to examine the topologically nontrivial behavior. This evaluation is particularly useful when the many-body wave function is numerically not accessible. We use dynamical mean-field theory (DMFT) in order to solve the present many-body problem approximately [33]. In the context of topological systems, DMFT has been used in numerous studies in 2D [34–43] as well as 3D systems [44,45]. DMFT has been applied recently to WSMs: In Ref. [46], the nonlocal annihilation of WPs within the BZ has been observed which is impossible in the noninteracting case. Reference [47], on the other hand, investigated the influence of interactions in view of the negative magnetoresistance. The interacting WSM has also been treated in a renormalization analysis hosting an axion insulator phase and nematic order [48] as well as by the variational cluster approach to study of density wave instabilities [49]. Our focus lies on the topological properties of the many-body phases which we obtain. We find that the WSM is robust up to a critical interaction strength. In particular, we observe that the transition from a topologically nontrivial WSM to a trivial Mott insulator occurs through the emergence of pairs of quasiparticle bands and so-called blind bands. Here, the former are topologically nontrivial and cancel out the nontrivial properties of the original WSM while the latter are topologically trivial. This ultimately results in an overall topologically trivial Mott insulator.

The paper is structured as follows: In Sec. II, we introduce the model for a WSM and investigate its noninteracting properties. In Sec. III, we analyze the WSM-to-Mott-insulator transition of the interacting model. In Sec. IV, we compute topological properties as a function of the interaction strength. In Sec. V, we discuss the effective quasiparticle spectrum and elaborate on the interaction-induced WSM-to-Mott-insulator topological phase transition. In order to study correlation effects on the surface, we investigate the model with one open boundary in Sec. VI. Finally, we conclude in Sec. VII.

II. MODEL

We study the tight-binding model proposed by Dubček *et al.* [50] which is motivated by the experimental

implementation of the Hofstadter model in Ref. [11], extended to three spatial dimensions. The corresponding real-space Hamiltonian for a single spin state τ reads as

$$\hat{H}_\tau = - \sum_j [(-1)^{x+y} K_x \hat{c}_{j+\hat{x},\tau}^\dagger \hat{c}_{j,\tau} + J_y \hat{c}_{j+\hat{y},\tau}^\dagger \hat{c}_{j,\tau} + (-1)^{x+y} K_z \hat{c}_{j+\hat{z},\tau}^\dagger \hat{c}_{j,\tau} + \text{H.c.}], \quad (1)$$

where $\mathbf{j} = (x, y, z)$ is a 3D lattice vector on a cubic lattice, $\hat{c}_{\mathbf{j},\tau}$ ($\hat{c}_{\mathbf{j},\tau}^\dagger$) annihilates (creates) a spin- τ fermion, with $\tau = \uparrow, \downarrow$, at lattice site \mathbf{j} , and $\hat{\mathbf{v}}$ denotes the unit vector in v direction. In the following, we focus on the isotropic case and set the hopping energies to the unit of energy $K_x = J_y = K_z = 1$. The momentum-space Hamiltonian is defined as $\hat{H}_\tau = \int d\mathbf{k} \hat{\mathbf{d}}_{\mathbf{k},\tau}^\dagger H(\mathbf{k}) \hat{\mathbf{d}}_{\mathbf{k},\tau}$ where $\hat{\mathbf{d}}_{\mathbf{k},\tau}$ is a two-component annihilation operator acting on the two sublattices (see Appendix A), with $H(\mathbf{k})$ given by

$$H(\mathbf{k}) = -2[\cos(k_x)\sigma^x + \sin(k_x)\sigma^y - \cos(k_z)\sigma^z]. \quad (2)$$

Here, we have set the lattice constant to unity. Also, the Pauli matrices σ^v refer to the pseudospin space of the two sites of the unit cell which breaks inversion symmetry. Details of the derivation of the Hamiltonian in Eq. (2) are provided in Appendix A. We read off four degeneracies of the Hamiltonian in Eq. (2) at the points $(k_x, k_y, k_z) = (0, \pm\pi/2, \pm\pi/2)$ in the first BZ. To confirm whether these degeneracies are indeed WPs, we compute the Chern number on a closed surface around a single degeneracy using Fukui's method [51]. In fact, any smooth closed surface can be used (see Appendix B). Indeed, the four points $(0, \pm\pi/2, \pm\pi/2)$ exhibit nonzero Chern numbers (+1 or -1), also dubbed *topological charge*. The sum over the four topological charges is zero.

III. MOTT TRANSITION

Let us now focus on the properties of the Mott transition of the model in Eq. (1). We consider fermions with a Hubbard interaction term $U \sum_j \hat{n}_{j,\uparrow} \hat{n}_{j,\downarrow}$ where U is the interaction strength and $\hat{n}_{j,\tau} = \hat{c}_{j,\tau}^\dagger \hat{c}_{j,\tau}$ is the particle-number operator of a spin- τ fermion on lattice site \mathbf{j} . Spin states are introduced in the following way in the four-band interacting Hamiltonian:

$$\hat{H}_{\text{int}} = \sum_\tau \hat{H}_\tau + U \sum_j \hat{n}_{j,\uparrow} \hat{n}_{j,\downarrow}. \quad (3)$$

The spin degeneracy results in a factor of 2 for the topological charges of the WPs.

One of the most successful methods for investigating Hubbard-type Hamiltonians and describing their Mott transitions is dynamical mean-field theory (DMFT) [33]. It maps the full Hubbard model onto a set of coupled self-consistent quantum impurity models which can be solved through different approaches like quantum Monte Carlo [52] or exact diagonalization [53] (ED). This mapping neglects nonlocal fluctuations but keeps track of all local quantum fluctuations. This manifests in a momentum-independent self-energy $\Sigma^{\tau\tau'}(\omega, \mathbf{k}) = \Sigma^{\tau\tau'}(\omega)$ with τ and τ' denoting spin states. In real space this means that the self-energy is local $\Sigma_{jl}^{\tau\tau'}(\omega) = \Sigma_j^{\tau\tau'}(\omega) \delta_{jl}$ where δ_{jl} is the Kronecker delta and \mathbf{j} and \mathbf{l} are

lattice vectors. As in static mean-field theories, DMFT is solved self-consistently and thus depends on an initial guess.

Here, we perform real-space DMFT [54,55] calculations on a $6 \times 6 \times 6$ lattice for the model in Eq. (3) with an ED solver with four bath sites. In real-space DMFT the Dyson equation in real space is used to compute the interacting Green's function in contrast to standard DMFT which is formulated in momentum space:

$$[G^{-1}(\omega)]_{jl}^{\tau\tau'} = [G_0^{-1}(\omega)]_{jl}^{\tau\tau'} - \Sigma_{jj}^{\tau\tau'}(\omega)\delta_{jl}. \quad (4)$$

Here, $G_0(\omega)$ is the noninteracting Green's function which can readily be computed from the noninteracting Hamiltonian. In our case the Green's function is a matrix of size $2 \times 6^3 \times 2 \times 6^3$ where the 2 inherits from the spin degree of freedom. This means there are 4×6^3 terms which are diagonal in real space. This number can be strongly reduced depending on the symmetries of the system and on the allowed magnetic solutions.

We are interested in the paramagnetic case. The paramagnetic solution is sufficient to describe the Mott transition. Besides, the temperature regimes we consider are above the superexchange temperature for antiferromagnetic ordering. The paramagnetic solution is found if diagonal elements of the self-energy in spin space are identical and off-diagonal elements vanish:

$$\Sigma_{jj}^{\uparrow\uparrow}(\omega) = \Sigma_{jj}^{\downarrow\downarrow}(\omega) \equiv \Sigma_{jj}(\omega), \quad (5)$$

$$\Sigma_{jj}^{\uparrow\downarrow}(\omega) = \Sigma_{jj}^{\downarrow\uparrow}(\omega) = 0. \quad (6)$$

To lowest order in the interaction strength, i.e., Hartree-Fock, the diagonal self-energies would be responsible for a S^z magnetization corresponding to the Hartree terms and the off-diagonal self-energies for the S^x and S^y magnetization corresponding to the Fock terms. Restricting to the paramagnetic solutions reduces the number of local self-energies which have to be computed to 6^3 .

The Hamiltonian in Eq. (3) is symmetric under the translations $\mathbf{j} \rightarrow \mathbf{j} + \hat{z}$ and $\mathbf{j} \rightarrow \mathbf{j} + \hat{x} + \hat{y}$. It is then sufficient to compute only two separate local self-energies instead of 6^3 , i.e., solving two separate impurity problems, and copy them accordingly in the lattice Green's function.

As indicators for the Mott transition, we compute two quantities: (i) the double occupancy

$$n_d = \frac{1}{N_s} \sum_j \langle \hat{n}_{\uparrow,j} \hat{n}_{\downarrow,j} \rangle, \quad (7)$$

where N_s is the number of lattice sites and $\langle \dots \rangle$ denotes the ensemble average; (ii) the quasiparticle weight [33], defined as

$$Q = \left[1 - \left. \frac{\partial \Sigma(\omega)}{\partial \omega} \right|_{\omega=0} \right]^{-1} = \left[1 - \left. \frac{\Sigma(i\omega_n)}{i\omega_n} \right|_{n=0} \right]^{-1}, \quad (8)$$

where we have introduced the real-frequency self-energy $\Sigma(\omega)$ and the self-energy in terms of Matsubara frequencies $\Sigma(i\omega_n)$. Here, Σ without any real-space coordinate refers to the average over the two-site unit cell. In practice, our results showed no difference between the two sites of the unit cell. For examples of the resulting selfenergy from DMFT, consult Appendix C.

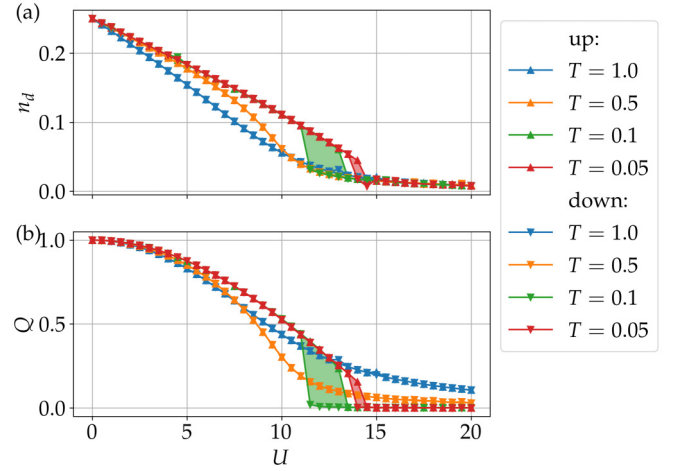


FIG. 1. Double occupancy n_d in (a) and quasiparticle weight Q in (b) as functions of the interaction strength U for different temperatures T . The direction of consecutive initial guesses for the self-energy for the DMFT calculations is labeled by *up* and *down*. The hysteresis between those is highlighted by a shaded area. Energies are measured in units of the hopping energy.

We present the results for n_d and Q in Fig. 1 as functions of the interaction strength U for different temperatures. The self-consistent solutions are found successively for different U . The initial guess for the self-consistent DMFT iteration is inherited from the previous converged solution for the previous value of U . Starting with $U = 0$, i.e., going upwards, the first guess for the initial self-energy is zero. For the downwards calculations, the deep Mott solution at $U = 20$ was used which was previously found by the upwards calculation. As the difference between those curves, we observe the typical hysteresis of the paramagnetic solutions shown as shaded areas [33]. The hysteresis reflects the coexistence of two solutions, i.e., the correlated WSM and the Mott insulator. The critical interaction strength for this phase transition is located within this coexistence regime. As we observe in Fig. 1, this regime is temperature dependent, and thus also the critical interaction strength. For comparison, the critical interaction strength for the metal-to-Mott-insulator transition in the 3D Hubbard model at $T \approx 0.33$ is $U = 15.4$ [56]. Hysteresis curves appear if a first-order phase transition is present. The first-order transitions from topological insulator phases to Mott insulators have been confirmed by Refs. [37,40,57] in 2D and 3D.

To determine transport properties of the obtained many-body phases, we are interested in the density of states

$$A(\omega) = -\frac{1}{\pi} \text{Im} \int d\mathbf{k} \text{Tr} G(\omega, \mathbf{k}), \quad (9)$$

where we have defined the retarded, real-frequency single-particle Green's function

$$G(\omega, \mathbf{k}) = \frac{1}{[\omega + 0^+ - \Sigma(\omega) + \mu] \mathbb{1} - H(\mathbf{k})}, \quad (10)$$

which does only apply for the paramagnetic solutions. Here, $\mathbb{1}$ denotes the 2×2 identity matrix in the sublattice representation, and μ is the chemical potential which is set to

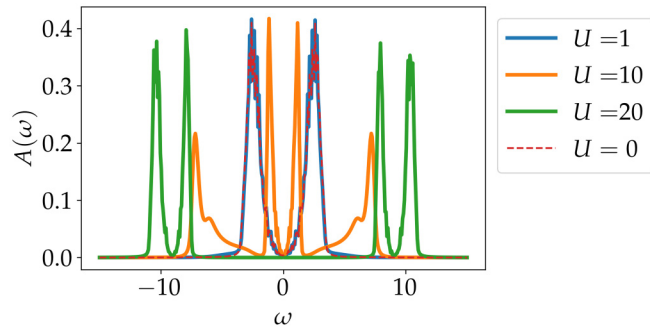


FIG. 2. Density of states $A(\omega)$ as a function of the frequency ω for different U at $T = 0.1$.

$U/2$ throughout the paper, constraining the system to be half-filled. In Fig. 2, we show the density of states for different U at $T = 0.1$. For $U = 1$, the density of states is almost identical to the one of the noninteracting case $U = 0$. This is expected since the self-energy is small in this regime. We also observe the peaks from the two bands of the Hamiltonian and an approximately quadratic behavior around $\omega = 0$ which is a property of a semimetal. For $U = 10$, we observe two Hubbard bands at approximately $\omega = \pm 8$. The bands close to $\omega = 0$ are shrunk compared to the $U = 1$ case but the system is still semimetallic. For $U = 20$, we find an overall gap of size ~ 16 which corresponds to the Mott gap. The structure of each of the Hubbard bands resembles the structure of the original density of states at $U = 0$. Such splitting of the noninteracting bands, each with the density of states similar to the noninteracting one, has been observed before in a bosonic system [36].

In Eq. (10), the self-energy in terms of real frequencies ω enters. While there are methods which are formulated in real frequencies [58], most impurity solvers provide the output as a function of Matsubara frequencies $i\omega_n$. Here, we use the maximum entropy method [59] in order to map $\Sigma(i\omega_n)$ to $\Sigma(\omega)$ (see Appendix C for comparison). This method was originally developed to analytically continue noisy quantum Monte Carlo data. It has the advantage to yield smooth outcomes through Bayesian statistics. Here, we use this method to analytically continue ED results. Conventionally, the density of states from ED calculations is rugged due to the finite number of bath sites. Here, the maximum entropy method can compensate that. Of course, the result is then approximate. The results in Fig. 2 show that our approach of combining the maximum entropy method with ED results yields a reasonable outcome.

In summary, the double occupancy, the quasiparticle weight, and the density of states provide clear evidence that the many-body phase for strong $U > 15$ is a Mott insulator. Let us now turn to the topological properties of the interacting system.

IV. ISHIKAWA-MATSUYAMA FORMULA

In 2D, the Ishikawa-Matsuyama formula manifests the generalization of a Chern number to interacting systems as it corresponds to the Hall conductivity up to a constant factor

and is formulated in terms of Green's functions [60]:

$$C_{\text{IM}} = \frac{\epsilon^{\nu\rho\eta}}{24\pi^2} \int dk \text{Tr}\{[G\partial_\nu G^{-1}][G\partial_\rho G^{-1}][G\partial_\eta G^{-1}]\}, \quad (11)$$

where $k = (k_0, k_1, k_2)$ with $k_0 = i\omega_n$ and ν, ρ, η run over the elements of k . k_1 and k_2 refer to the momenta of the two spatial dimensions in 2D. We also have used the abbreviation $G = G(k) = G(i\omega_n, k_1, k_2)$ in Eq. (11). The formula is rather complicated compared to the noninteracting Thouless-Kohmoto-Nightingale-den Nijs (TKNN) invariant [61]. It has been shown, however, that in some regimes the information about the full frequency range is not necessary and only the $\omega = 0$ mode is crucial [62]. This is called the effective topological Hamiltonian approach which makes it possible to compute topological invariants from an effective, noninteracting Hamiltonian $H_{\text{top}} = -G^{-1}(\omega = 0, \mathbf{k})$. This, however, is valid only if the Green's function has no zeros which is of course not the case in a Mott insulator. Thus, we have to consult the formula in Eq. (11). To this end, we define the single-particle Green's function within the DMFT framework, i.e., $\Sigma(i\omega_n, \mathbf{k}) = \Sigma(i\omega_n)$, according to Ref. [63]:

$$G(i\omega_n, k_1, k_2) = \frac{1}{[i\omega_n - \Sigma(i\omega_n) + \mu]\mathbb{1} - H(k_1, k_2)}. \quad (12)$$

For the sake of brevity, we drop all the arguments. So, we find

$$\partial_{k_0} G^{-1} = (1 - \partial_{k_0} \Sigma)\mathbb{1} = (1 + i\partial_{\omega_n} \Sigma)\mathbb{1}, \quad (13)$$

$$\partial_{k_\nu} G^{-1} = \partial_{k_\nu} H = j_\nu, \quad (14)$$

where $j_\nu = j_\nu(k_1, k_2)$ is the current in $\nu = 1, 2$ direction with the 2D momenta k_1 and k_2 . Consequently, Eq. (11) simplifies to

$$C_{\text{IM}} = \frac{i}{8\pi^2} \int dk_1 dk_2 d\omega_n \text{Tr}[G j_1 G j_2 G (1 + i\partial_{\omega_n} \Sigma) - (1 + i\partial_{\omega_n} \Sigma) G j_2 G j_1 G]. \quad (15)$$

In order to apply this formula in our 2D model, we again embed a closed 2D surface in the 3D BZ. Following the above discussion of the noninteracting case (see also Appendix B), we will put the 2D momentum (k_1, k_2) onto a surface enclosing the WPs in the 3D BZ of the interacting system to compute topological charges of the WPs in the interacting case. To see the functional relation between the 2D surface momenta (k_1, k_2) and the 3D momenta (k_x, k_y, k_z) , consult Appendix B.

The momentum-dependent part of the formula in Eq. (15) can be calculated analytically depending on the surface enclosing the WP over which we want to integrate. For the two components of the currents, this implies

$$j_r = \sum_\nu j_\nu \frac{\partial k_\nu}{\partial k_r}, \quad r = 1, 2 \text{ and } \nu = x, y, z. \quad (16)$$

The frequency derivative is performed numerically as

$$\partial_{\omega_n} \Sigma(i\omega_n) \approx \frac{\Sigma(i\omega_{n+1}) - \Sigma(i\omega_n)}{2\pi T}, \quad (17)$$

according to the definition of the fermionic Matsubara frequencies $\omega_n = \pi T(2n + 1)$ with n being an integer. Before computing the topological charge of the interacting system by enclosing the WPs with a surface, we have to find their

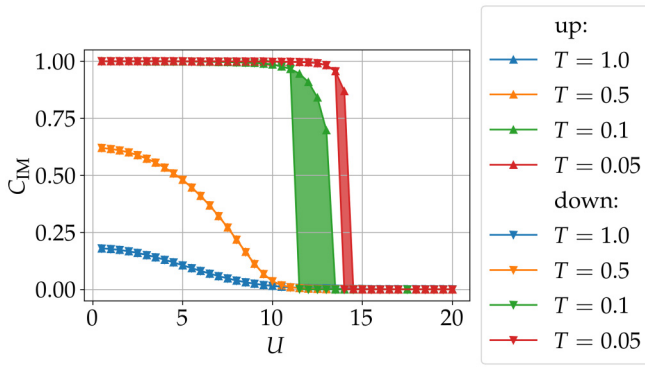


FIG. 3. Ishikawa-Matsuyama invariant C_{IM} for the interacting Hamiltonian in Eq. (3) as a function of U for different temperatures on a sphere in the BZ with radius $R_S = \pi/2$ enclosing the WP at $\mathbf{k}_{\text{WP}} = (0, \pi/2, \pi/2)$ for one spin state. Here, we again highlight the hysteresis by a shaded area.

position within the BZ as a function of U because their position could, in general, depend on the interaction. To this end, we maximize the imaginary part of the Green's function at the Fermi level $-\text{Im Tr}G(\omega = 0, \mathbf{k})$ which corresponds to the contribution to the density of states [see Eq. (9)]. The obtained momentum yields the position of the WPs. Interestingly, as the result, we find that the position of the WPs does not depend on the strength of the interaction, which is not shown here. However, we note that the inclusion of a staggered potential as, e.g., in Ref. [39], might change this since it is another energy scale competing with the interaction strength. Also note that the described procedure of determining the positions of the WPs does not rely on an effective noninteracting theory, in contrast to the procedure of Ref. [46].

In Fig. 3, we show the Ishikawa-Matsuyama invariant C_{IM} calculated on a sphere with radius $R_S = \pi/2$ enclosing the WP at $\mathbf{k}_{\text{WP}} = (0, \pi/2, \pi/2)$. For moderate as well as large U , we find well-quantized results. Close to the Mott transition, the C_{IM} is not quantized anymore. This is due to the finite temperature which becomes comparable to the gap in the vicinity of the phase transition (see Fig. 2). The result in Fig. 3 is comparable to a result of a similar DMFT study of the Bernevig-Hughes-Zhang model [64].

V. QUASIPARTICLE SPECTRUM AND BLIND BANDS

It is anticipated that the topological invariant on the enclosing surface vanishes when the WPs gap out since the system then lacks the singularity which has to be enclosed (compare Figs. 2 and 3). The resulting many-body state is globally gapped. Due to the lack of WPs there are neither sources nor sinks of Berry curvature. The many-body state is thus topologically trivial. For finite magnetization, topologically trivial [34,39] as well as nontrivial [65–69] states have been found.

We want to understand in more detail how this topological phase transition to a topologically trivial Mott insulator occurs. To this end, we again focus on the paramagnetic case. Our conventional understanding of topological phase transitions is the closing of a quasiparticle band gap. Quasiparticle bands exhibit Chern numbers and correspond to the poles of

the single-particle Green's function. It has been discussed, however, on the level of single-particle Green's functions, that not only poles of the Green's function can exhibit nontrivial Chern numbers but also zeros of the Green's function. The zeros of the Green's function are dubbed *blind bands*. Reference [70] proposed the interaction-induced topological phase transition through a gap closing of blind bands. Herein, not only the quasiparticle bands, but also the blind bands exhibit nontrivial Chern numbers. The gap closing of blind bands then can induce a topological phase transition. In our case, we do not find nontrivial blind bands but rather a topological phase transition stemming from the quasiparticle bands only.

The topological properties of the interacting system are described by a formula for a generalized Chern number \tilde{C} which relates the Chern numbers of quasiparticle bands and the Chern numbers of blind bands and was derived from the Ishikawa-Matsuyama formula [41]:

$$\begin{aligned} \tilde{C} = & \sum_{n=1}^N \int dk_1 dk_2 \text{Im} \langle \partial_{k_1} \psi(\omega_n^p(\mathbf{k}), \mathbf{k}) | \partial_{k_2} \psi(\omega_n^p(\mathbf{k}), \mathbf{k}) \rangle \\ & - \sum_{m=1}^M \int dk_1 dk_2 \text{Im} \langle \partial_{k_1} \psi(\omega_m^z(\mathbf{k}), \mathbf{k}) | \partial_{k_2} \psi(\omega_m^z(\mathbf{k}), \mathbf{k}) \rangle. \end{aligned} \quad (18)$$

Herein, we have defined the eigenstates $|\psi_j(\omega, \mathbf{k})\rangle$ of the Green's function according to

$$G(\omega, \mathbf{k}) |\psi_j(\omega, \mathbf{k})\rangle = g_j(\omega, \mathbf{k}) |\psi_j(\omega, \mathbf{k})\rangle. \quad (19)$$

Since the Green's function is not Hermitian away from $\omega = 0$, the eigenvalues $g_j(\omega, \mathbf{k})$ are not real in general and there is no generic ordering. Since we are only interested in zeros and poles of $g_j(\omega, \mathbf{k})$, we order the eigenvalues by their absolute values. In Eq. (18), we have also defined the quasiparticle bands $\omega_n^p(\mathbf{k})$ and the blind bands $\omega_m^z(\mathbf{k})$ as the poles and zeros of the Green's function, respectively:

$$g_j(\omega = \omega_n^p(\mathbf{k}), \mathbf{k}) \rightarrow \infty \text{ and } g_j(\omega = \omega_m^z(\mathbf{k}), \mathbf{k}) = 0. \quad (20)$$

We have dropped the band index j for the states in Eq. (18) since j is fully determined by $\omega_n^p(\mathbf{k})$ and $\omega_m^z(\mathbf{k})$, respectively. Furthermore, we focus on the weakly interacting case and the deep Mott-insulating case. In the intermediate regime, the poles and zeros are not sufficiently pronounced. Note that the physics in the deep Mott regime will certainly differ from this treatment as, e.g., particle-hole excitations are neglected. We emphasize that our discussion focuses on the framework of single-particle Green's functions.

We show the absolute value of the eigenvalues of the Green's function in Fig. 4 as a function of ω exemplarily for $(k_1, k_2) = (0, 0)$ on the WP-enclosing sphere which corresponds to $\mathbf{k} = (0, \pi/2, \pi)$ (see Appendix B for details). For $U = 1$, there are two poles corresponding to two quasiparticle bands. These bands approximately correspond to the noninteracting energy bands since the interaction is small compared to the bandwidth. Poles in this plot are finite since we use a finite broadening factor η in the analytically continued Green's function $G(\omega + i\eta, \mathbf{k})$ with the definition in Eq. (12). Also, the exact pole will not be matched perfectly because of the equidistant discretization of the frequency axis. For $U = 20$,

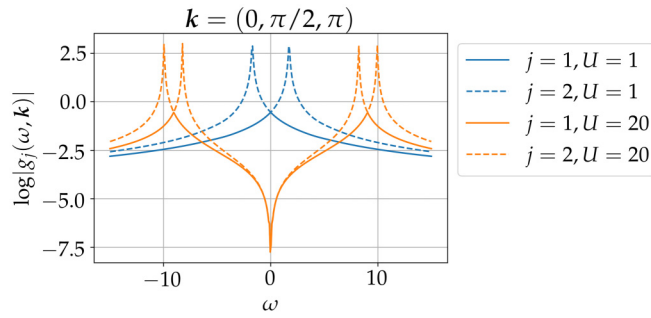


FIG. 4. Absolute value of the eigenvalues of the Green's function in log scale exemplarily for a specific \mathbf{k} on the WP-enclosing sphere.

we observe four poles and additionally a zero at $\omega \approx 0$. We also observe that the zero is doubly degenerate.

In Fig. 5, we show the numerically determined momentum-resolved quasiparticle bands $\omega_h^p(\mathbf{k})$ in blue and blind bands $\omega_m^z(\mathbf{k})$ in orange of the single-particle Green's function. The respective Chern number C is computed with the Fukui method [51] and is written next to the band. For $U = 1$, the spectrum resembles that of the noninteracting case which is expected for such small interaction strength. Also, the Fermi level lies between the two bands which carry opposite nontrivial Chern numbers. This is consistent with a topologically nontrivial many-body phase (see Fig. 3).

For $U = 20$, we observe four quasiparticle bands and a twofold-degenerate blind band. This shows the preserved difference $N - M$ between the number of quasiparticle bands and the number of blind bands. We also note that the blind band is flat. This is because in the single-particle Green's function (12), a zero emerges only if the self-energy diverges. As the self-energy is momentum independent within DMFT, the blind band has no momentum dependence and is thus flat. Additionally, the blind bands contribute zero Chern number to the total Chern number. Out of the four quasiparticle bands, the lower two are occupied which have opposite Chern numbers. The total Chern number is thus zero which is consistent with the obtained topologically trivial Mott insulator (see Fig. 3). Each of the Hubbard bands consists of subbands with the same quasiparticle spectrum as the original

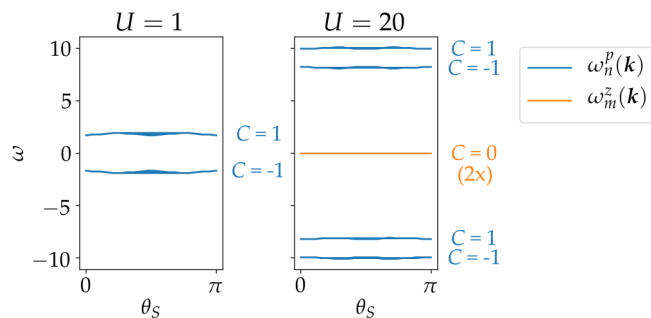


FIG. 5. Quasiparticle bands $\omega_h^p(\mathbf{k})$ and blind bands $\omega_m^z(\mathbf{k})$ of the single-particle Green's function on a sphere with radius $R_S = \pi/2$ enclosing the WP at $(0, \pi/2, \pi/2)$ in the BZ. The Chern number C is written next to the respective band. Note that this 2D plot shows a function of the azimuth $k_1 = \theta_S$ only. Values as a function of the polar angle are plotted implicitly on top of each other.

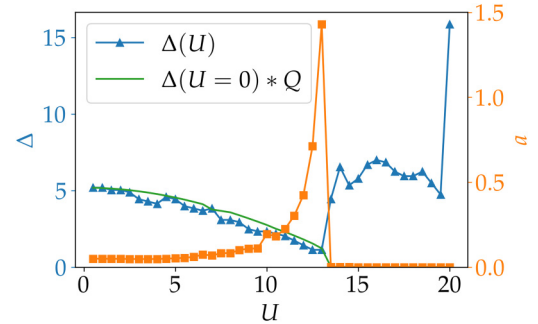


FIG. 6. Quantification of the density of states on a sphere with radius $R_S = \pi/2$ enclosing the WP at $(0, \pi/2, \pi/2)$ in the BZ: distance Δ between peaks of the density of states $A(\omega)$ closest to $\omega = 0$ and quadratic fitting coefficient a of $A(\omega) \approx a\omega^2$ at $\omega \approx 0$ as a function of U for $T = 0.1$. We also plot $\Delta(U = 0) * Q$ with the data from Fig. 1(b) which is an approximation for Δ .

noninteracting band structure. Since the sum of Chern numbers of all the bands in the original band structure is zero, the Hubbard bands are topologically trivial as well. This is similar to the topologically trivial Mott insulator found in the bosonic Haldane-Hubbard model studied with DMFT which showed the equivalent structure of subbands [36].

We conclude that in our situation, the topological Mott transition does not occur due to an emerging topologically nontrivial blind band which crosses the gap as suggested by Ref. [70] for a possible interaction-induced topological phase transition. Rather, the topological properties stem fully from the quasiparticle bands. This requires a closing of the quasiparticle band gap. To see this quantitatively, we compute two new quantities derived from the density of states $A(\omega)$: (i) the distance between the peaks of $A(\omega)$ closest to $\omega = 0$ which we denote Δ . It is qualitatively equivalent to the gap of the quasiparticle bands of the the 2D sphere in the 3D BZ surrounding the WP. (ii) the coefficient of a quadratic fit of the spectral function $A(\omega) \approx a\omega^2$ at $\omega \approx 0$. The coefficient a is useful since it reflects the property of a semimetal that the density of states vanishes at $\omega = 0$. In Fig. 6, we show Δ as well as a as a function of U . We indeed observe towards the expected topological phase transition point at $U \approx 13$ that Δ decreases and approximately without reaching zero. At the same time a increases and becomes large close to $U \approx 13$. Both indicate a closing of a quasiparticle gap as well as a flattening of the the semimetallic quasiparticle bands which ultimately ends in a first-order transition. In the Fermi-liquid regime, the value of Δ can be approximated by the quasiparticle weight. In Fig. 6, we plot the product of the noninteracting value of Δ and the quasiparticle weight Q according to Fig. 1(b).

As we discussed before, the WPs do not move in the BZ while tuning the interaction strength. In the considered cases the topological phase transition is first order. First-order transitions generally end in a critical point where the transition becomes second order. The first-order transition occurs inside a coexistence region in the $T-U$ phase diagram where both the Fermi liquid and the Mott insulator are solutions. The critical interaction strength $U_{c1}(T)$ marks the beginning and critical interaction strength $U_{c2}(T)$ marks the end of the coexistence region. At the point where $U_{c1}(T) = U_{c2}(T)$, the

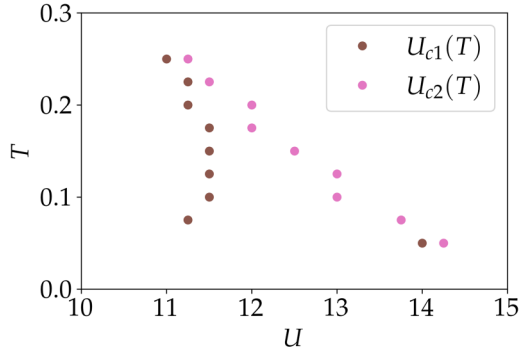


FIG. 7. Coexistence regime of Fermi-liquid and Mott-insulator solutions. U_{c1} marks where the hysteresis begins and U_{c2} where it ends. For small temperatures, the coexistence region shrinks abruptly. This we account to the DMFT algorithm at very low temperatures.

critical point where the phase transition becomes second order is located. In order to determine the coexistence region approximately, we perform DMFT calculations with a better resolution compared to Fig. 1. This is done for the upwards as well as the downwards DMFT procedure. We then calculate the difference of quasiparticle weight between both directions $Q_{\text{up}}(T, U) - Q_{\text{down}}(T, U)$. The points in the phase diagram where this quantity is larger (smaller) than some threshold determine $U_{c1}(T)$ [$U_{c2}(T)$]. We choose 10% for the threshold in order to get rid of numerical noise. The result is shown in Fig. 7. From there, we read off that the critical point could be located approximately at $(T \approx 0.3, U \approx 11)$. For $T = 0.05$, the coexistence region shrinks abruptly. We assume that this stems from underfitting in the ED solver at small temperatures.

VI. SURFACE STATES

We now investigate surface states of the Dubček model with Hubbard interaction. To this end, we run real-space DMFT calculations where in two directions we apply periodic

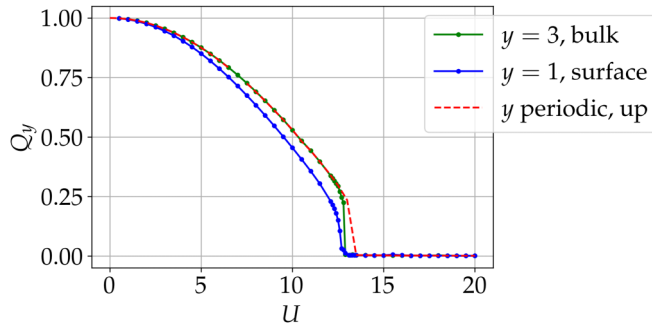


FIG. 8. Quasiparticle weight in the bulk and at the surface as a function of the interaction strength U at $T = 0.1$. For comparison, we plot Q as a function of U in the y -periodic system according to the data in Fig. 1(b). The results correspond to the upwards computations of the DMFT algorithm. Since the downwards calculation will presumably not show the interesting features around $U = 12.8$, we do not show them here.

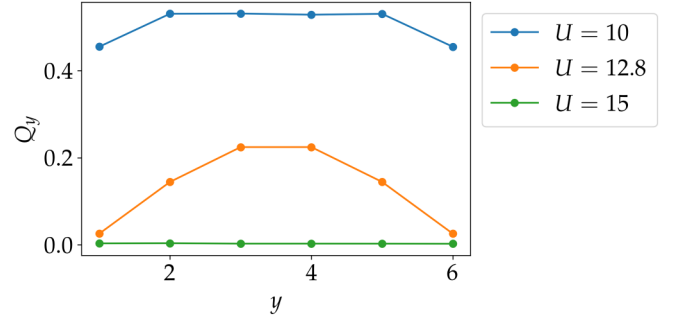


FIG. 9. Quasiparticle weight resolved with respect to the real-space coordinate y for three different interaction strengths.

boundary condition and in the third direction we apply open boundary conditions. In this manner, three different configurations of boundary conditions are thinkable. Our results, however, did not show any difference in the physics between these three configurations. Thus, for the discussion we focus on the case where the x and z directions are extended and in the y direction the system is finite with N_y lattice sites. The noninteracting Hamiltonian in this configuration is $\hat{H}_\tau = \int dk_x dk_z \hat{H}_\tau(k_x, k_z)$ with $\hat{H}_\tau(k_x, k_z)$ given by

$$\begin{aligned} \hat{H}_\tau(k_x, k_z) = & -J_y \sum_{y=1}^{N_y-1} (\hat{c}_{\tau, y+1, k_x, k_z}^\dagger \hat{c}_{\tau, y, k_x, k_z} + \text{H.c.}) \mathbb{1} \\ & - 2 \sum_{y=1}^{N_y} (-1)^y \hat{c}_{\tau, y, k_x, k_z}^\dagger \hat{c}_{\tau, y, k_x, k_z} \\ & \times [K_x \sin(k_x) \sigma^y + K_z \cos(k_z) \sigma^z], \end{aligned} \quad (21)$$

which, in matrix representation, is a matrix of size $2N_y \times 2N_y$. Here, N_y corresponds to the size of the system in y direction and the 2 stems from a small two-site unit cell in x direction to which the Pauli matrices apply. The Hamiltonian in Eq. (21) can be derived by following the derivation in Appendix A and omitting the Fourier transform in y direction.

From the paramagnetic DMFT calculations we obtain in this configuration a self-energy $\Sigma_y(i\omega_n)$ and $\Sigma_y(\omega)$ which is position resolved in the y direction. We performed DMFT calculations for $N_y = 6$. In order to quantify correlation effects,

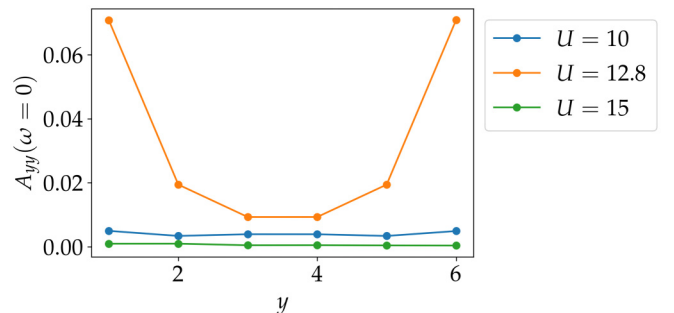


FIG. 10. y -resolved spectral function at the Fermi level $A_{yy}(\omega = 0)$ for three different values of U .

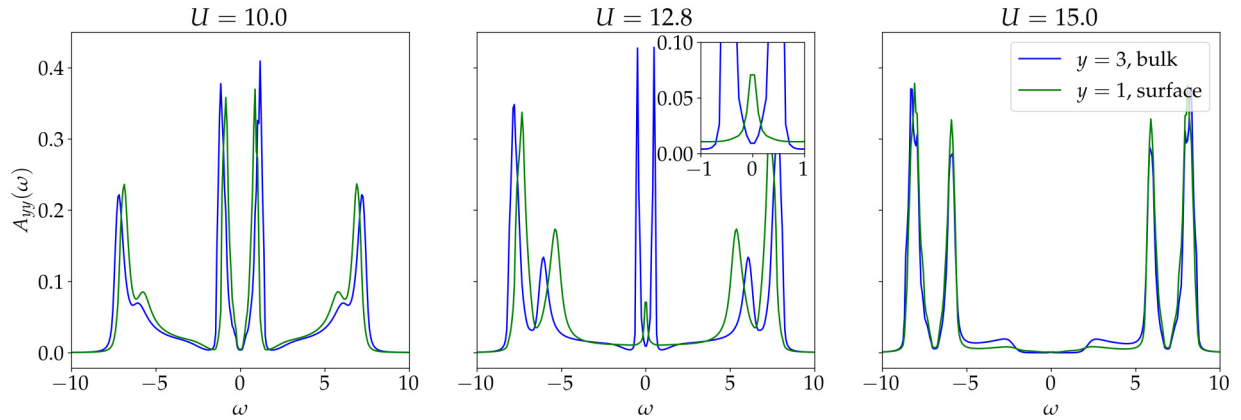


FIG. 11. Spectral function $A(\omega)$ in the bulk and at the surface for three different values of U : showing semi-metallic Fermi liquid behavior at $U = 10$, Mott-insulating behavior at $U = 15$, and the correlated surface states at $U = 12.8$. The inset corresponds to a zoom of the correlated surface states.

we define the y -resolved quasiparticle weight

$$Q_y = \left[1 - \frac{\Sigma_y(i\omega_n)}{i\omega_n} \Big|_{n=0} \right]^{-1} \quad (22)$$

as well as the y -resolved spectral density

$$A_{yy}(\omega) = -\frac{1}{\pi} \text{Im} \int dk_x dk_z \times \frac{1}{[\omega + 0^+ + \mu] \mathbb{1} - \text{diag}[\Sigma_y(\omega)] - H(k_x, k_z)} \Big|_{yy}, \quad (23)$$

where the Hamiltonian is represented in matrix representation and the self-energy is a diagonal matrix. In order to incorporate the two-site unit cell in the x direction, we average over those two sites. In Fig. 8, we present the y -resolved quasiparticle weight Q_y defined in Eq. (22) as a function of the interaction strength U for $y = 1$ and 3 , respectively. $y = 1$ is a site which is located directly at surface of the system and $y = 3 = N_y/2$ is presumably a bulk site. We compare the function $Q_{y=3}$ with the function Q of the extended system in which the y direction is also periodic. We observe that these two curves agree very well and conclude that $N_y = 6$ is a sufficiently large choice for the system. We furthermore observe the quasiparticle weight at the surface $Q_{y=1}$ is overall

smaller than the corresponding bulk value. There is even a regime in which Q_1 is much smaller and almost zero while Q_3 is still finite. Exemplarily, this occurs at $U = 12.8$. So we will focus on this value in the following and also $U = 10$ and 15 as reference values. These are highlighted in Fig. 8. In Fig. 9, we show the spatially resolved quasiparticle weight as a function of y for the three values of U . For $U = 10$, we observe that Q_y is finite for all sites, i.e., a semimetallic Fermi-liquid phase. For $U = 15$, we see that Q_y is zero for all sites, i.e., the system is in a Mott-insulating state for all sites in the y direction. For $U = 12.8$, we find a clear quantitative difference between bulk and surface, i.e., a bulk value of $Q_3 \approx 0.25$ and a surface value of $Q_1 \approx 0.025$.

Furthermore, we look at the spectral density at the Fermi level as a function of y in Fig. 10. It is important to note that the spectral density is normalized locally, i.e.,

$$\int d\omega A_{yy}(\omega) = 1 \text{ for every } y. \quad (24)$$

We observe that for the cases $U = 10$ and 15 , the spectral density is low at the Fermi energy in the bulk as one expects from a semimetal. Also, it seems that at the surface the spectral density is not much different from the bulk value. This suggests that there might not be metallic states like Fermi arcs present. In fact, for the Dubček model [50], one expects Fermi arc states at the surface spanned by the unit vectors $(\hat{x} + \hat{y})/\sqrt{2}$ and \hat{z} . In our theory, we cannot address this surface and thus focus on the principal directions. For the case of $U = 12.8$ in Fig. 10, the spectral density of the Fermi level is larger at $U = 12.8$ than for $U = 10$ or 15 . Also, one can identify a difference between the bulk density of states and the surface density of states. To understand better this phenomenon, we present the energy-resolved spectral density $A_{yy}(\omega)$ defined in Eq. (23) in Fig. 11 for the bulk $y = 3$ as well as the surface $y = 1$. For $U = 10$, we observe the Fermi-liquid regime, in which the semimetallic density of states is visible. Note that the surface density of states is shrunk with respect to the bulk density of states, i.e., peaks are shifted towards $\omega = 0$. For $U = 15$, bulk and surface densities of states approximately coincide and are gapped. For $U = 12.8$, we see a qualitative difference between the bulk and the surface density of states.

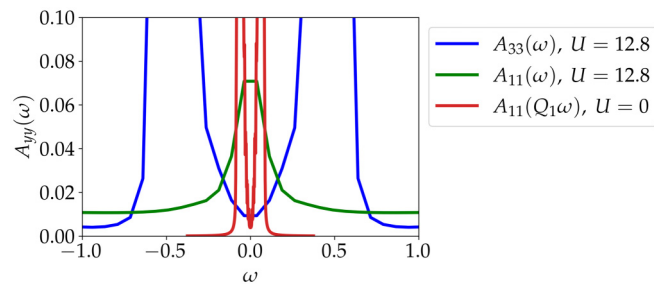


FIG. 12. The density of states $A_{yy}(\omega)$ according to Fig. 11 for $U = 12.8$ in comparison with the rescaled noninteracting density of states $A_{yy}(Q_1\omega)$ where Q_1 corresponds to the surface quasiparticle weight at $U = 12.8$.

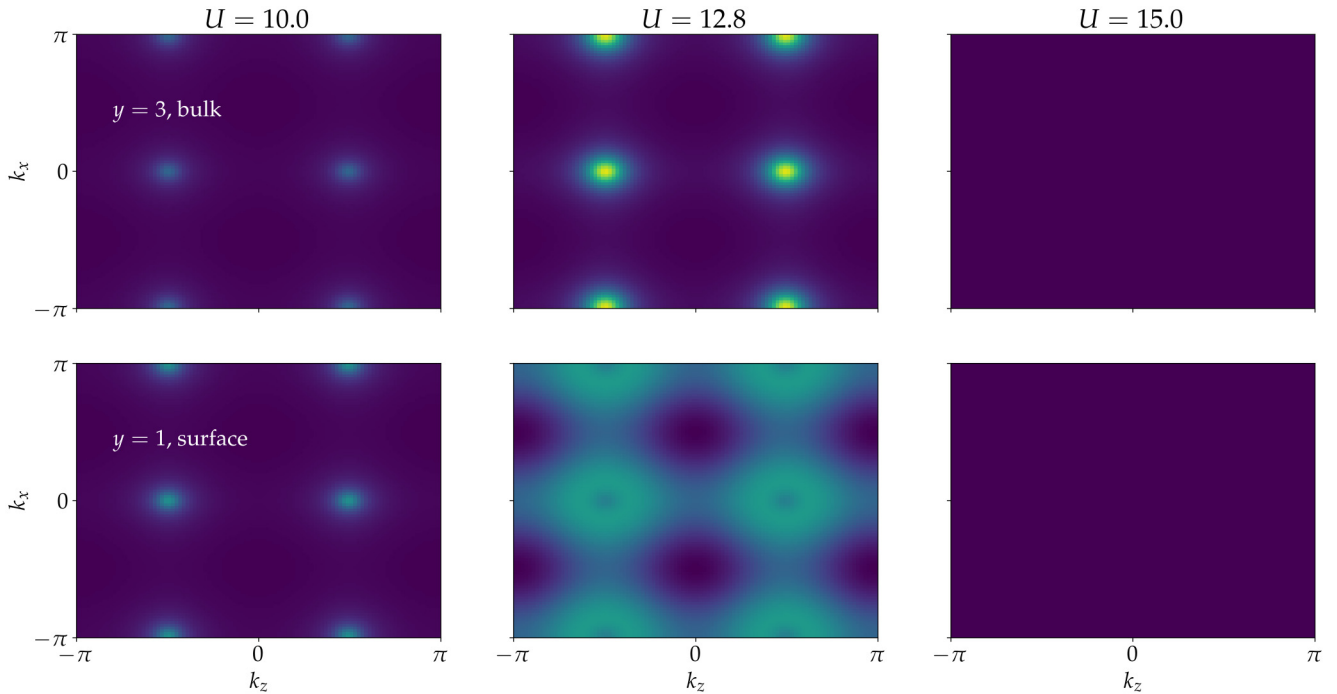


FIG. 13. Momentum-resolved spectral function at the Fermi level in the transversal BZ in the bulk and at the surface for three different values of U . Dark blue corresponds to zero and yellow to $0.1/(2\pi)^2$.

Here, the bulk density of states shows the semimetallic behavior we already know from the y -periodic system (see Fig. 9). The surface density of states, however, shows a metallic peak at the Fermi level which we enlarged in the inset of Fig. 11.

It is important to note that Q_1 at $U = 12.8$ does not vanish (see Fig. 9). We can use this value to rescale ω in the argument of the density of states of the noninteracting case [33] as we show in Fig. 12. The semimetallic density of states is squeezed together by a very small factor of $Q \approx 0.025$. This means that the two peaks of the semimetallic density of states come very close. Because of the interactions, the density of states also broadens at the same time. Thus, the broadening is strong enough to merge the two semimetallic peaks in the density of states into a single metallic peak at $\omega = 0$.

We are interested in the structure of the surface states which we have observed in Fig. 11. Therefore, we compute the spectral function within the transverse BZ for $\omega = 0$, i.e., spanned by the momenta k_x and k_y . This can be achieved by omitting the twofold momentum integration in Eq. (23). Note that this quantity is still normalized according to Eq. (24). We show the bulk transverse BZ at the Fermi level in the upper panel of Fig. 13. For $U = 10$, we observe the WPs which are visible because of a finite broadening. For $U = 12.8$, the WPs are more pronounced and at $U = 15$ they are completely gapped out by the Mott gap. The surface BZ is shown in the lower panel and for $U = 10$ and 15 , we observe a similar picture as in the bulk. In the case of $U = 12.8$, however, the structure of the spectral function within the BZ is different. Here, the surface spectral density between the positions of the bulk WPs is finite which suggests the existence of a metallic state. This is indeed what we anticipated from the analysis of the energy-resolved spectral function in Fig. 11. This state is fully connected, yet it geometrically differs from a Fermi

arc. Also, a Fermi arc is already visible in the single-particle spectrum of the noninteracting model [50] whereas for the present state strong interactions have to be applied. At this stage, it is, however, not clear what the impact of the finite size of the system is. Also, we have only presented results of the upwards direction of the DMFT iterations [see the discussion below Eq. (8)]. The present state is presumably not visible in the downward direction.

VII. CONCLUSION

We have investigated an experimentally relevant model in the field of cold atoms in optical lattices by means of DMFT. We have calculated the double occupancy, the quasiparticle weight, as well as the density of states to determine a paramagnetic Mott-insulating phase for strong Hubbard interactions. Through numerical evaluation of the Ishikawa-Matsuyama formula, which is more general than the effective topological Hamiltonian approach, we have determined the topological WSM-to-Mott-insulator transition. We investigated this topological phase transition in further detail by extracting quasiparticle bands and blind bands which both can carry Chern numbers. It turns out that the topological phase transition occurs through a first-order transition. This enables the nonlocal annihilation of the Weyl points. The flat blind bands do not contribute to the topological properties of the system. Ultimately, we have studied correlated surface physics by breaking the periodicity of the y direction. For weak and strong interaction strengths the system is completely semimetallic and Mott insulating, respectively. For a narrow region close to the topological phase transition, however, we find a correlated surface state which is metallic while the bulk

is semimetallic. This state is different from a Fermi arc as it requires strong interactions.

ACKNOWLEDGMENTS

The authors acknowledge enlightening discussions with M. Pasek and U. Gebert. This work was supported by the Deutsche Forschungsgemeinschaft (DFG, German Research Foundation) under Project No. 277974659 via Research Unit FOR 2414. This work was also supported by the DFG via the high performance computing center LOEWE-CSC. T. Grass acknowledges funding from “la Caixa” Foundation (ID No. 100010434, fellowship code No. LCF/BQ/PI19/11690013), ERC AdG NOQIA, Spanish Ministry MINECO and State Research Agency AEI (FIDEUA PID2019-106901GB-I00/10.13039/501100011033, SEVERO OCHOA No. SEV-2015-0522 and CEX2019-000910-S, FPI), European Social Fund, Fundacio Cellex, Fundacio Mir-Puig, Generalitat de Catalunya (AGAUR Grant No. 2017 SGR 1341, CERCA program, QuantumCAT U16-011424, co-funded by ERDF Operational Program of Catalonia 2014-2020), MINECO-EU QUANTERA MAQS [funded by State Research Agency (AEI) PCI2019-111828-2/10.13039/501100011033], EU Horizon 2020 FET-OPEN OPTOLogic (Grant No. 899794), and the National Science Centre, Poland-Symfonia Grant No. 2016/20/W/ST4/00314. J.-H. Zheng acknowledges the support from the Research Council of Norway through its Centres of Excellence funding scheme (Project No. 262633, “QuSpin”).

APPENDIX A: FOURIER TRANSFORM OF THE REAL-SPACE HAMILTONIAN

Here, we derive the compact form of the \mathbf{k} -space Hamiltonian in terms of Pauli matrices. To this end, we start from the real-space Hamiltonian defined in Eq. (1) and define two sublattices A and B , where A contains all the sites for which $x + y$ is even and B contains all the sites for which $x + y$ is odd. We find

$$\begin{aligned} \hat{H}_\tau = & - \sum_{j \in A} [K_x \hat{c}_{j+\hat{x},\tau}^\dagger \hat{c}_{j,\tau} + J_y \hat{c}_{j+\hat{y},\tau}^\dagger \hat{c}_{j,\tau} \\ & + K_z \hat{c}_{j+\hat{z},\tau}^\dagger \hat{c}_{j,\tau} + \text{H.c.}] \\ & - \sum_{j \in B} [-K_x \hat{c}_{j+\hat{x},\tau}^\dagger \hat{c}_{j,\tau} + J_y \hat{c}_{j+\hat{y},\tau}^\dagger \hat{c}_{j,\tau} \\ & - K_z \hat{c}_{j+\hat{z},\tau}^\dagger \hat{c}_{j,\tau} + \text{H.c.}], \end{aligned} \quad (\text{A1})$$

Now, we define two new sets of operators

$$\hat{c}_{j,\tau} = \begin{cases} \hat{a}_{j,\tau} & \text{if } j \in A, \\ \hat{b}_{j,\tau} & \text{if } j \in B, \end{cases} \quad (\text{A2})$$

which simplifies the Hamiltonian as

$$\begin{aligned} \hat{H}_\tau = & \sum_{j \in A} [-K_x \hat{b}_{j+\hat{x},\tau}^\dagger \hat{a}_{j,\tau} - J_y \hat{b}_{j+\hat{y},\tau}^\dagger \hat{a}_{j,\tau} \\ & - K_z \hat{a}_{j+\hat{z},\tau}^\dagger \hat{a}_{j,\tau} + K_x \hat{a}_{j+\hat{x},\tau}^\dagger \hat{b}_{j,\tau} \\ & - J_y \hat{a}_{j+\hat{y},\tau}^\dagger \hat{b}_{j,\tau} + K_z \hat{b}_{j+\hat{z},\tau}^\dagger \hat{b}_{j,\tau} + \text{H.c.}], \end{aligned} \quad (\text{A3})$$

Fourier transformation of the operators leads to

$$\begin{aligned} \hat{H}_\tau = & 2 \int d\mathbf{k} [-iK_x \sin(k_x) (\hat{a}_{\mathbf{k},\tau}^\dagger \hat{b}_{\mathbf{k},\tau} - \hat{b}_{\mathbf{k},\tau}^\dagger \hat{a}_{\mathbf{k},\tau}) \\ & - J_y \cos(k_y) (\hat{a}_{\mathbf{k},\tau}^\dagger \hat{b}_{\mathbf{k},\tau} + \hat{b}_{\mathbf{k},\tau}^\dagger \hat{a}_{\mathbf{k},\tau}) \\ & + K_z \cos(k_z) (\hat{a}_{\mathbf{k},\tau}^\dagger \hat{a}_{\mathbf{k},\tau} - \hat{b}_{\mathbf{k},\tau}^\dagger \hat{b}_{\mathbf{k},\tau})]. \end{aligned} \quad (\text{A4})$$

Defining the spinor operator $\hat{\mathbf{d}}_{\mathbf{k},\tau} = (\hat{a}_{\mathbf{k},\tau}, \hat{b}_{\mathbf{k},\tau})^T$ leads to

$$\begin{aligned} \hat{H}_\tau = & 2 \int d\mathbf{k} \hat{\mathbf{d}}_{\mathbf{k},\tau}^\dagger [K_x \sin(k_x) \sigma^y - J_y \cos(k_x) \sigma^y \\ & + K_z \cos(k_z) \sigma^z] \hat{\mathbf{d}}_{\mathbf{k},\tau}, \end{aligned} \quad (\text{A5})$$

which corresponds to the Hamiltonian in Eq. (2) given in the main text according to $\hat{H}_\tau = \int d\mathbf{k} \hat{\mathbf{d}}_{\mathbf{k},\tau}^\dagger H(\mathbf{k}) \hat{\mathbf{d}}_{\mathbf{k},\tau}$.

APPENDIX B: CHERN NUMBER IN CURVILINEAR COORDINATES

Here, we show that the analytical form of the Chern number stays invariant in an arbitrary 3D curvilinear coordinate system. We transform the expression for the Chern number which is typically defined in the Cartesian BZ (k_x, k_y, k_z) to the curvilinear coordinate system (k_1, k_2, k_3). The flux element reads as

$$B dS = d\mathbf{S} \cdot \partial_{\mathbf{k}} \times \mathbf{A}, \quad (\text{B1})$$

where $\mathbf{A} = i \langle \psi | \partial_{\mathbf{k}} | \psi \rangle$ is the Berry connection with $\partial_{\mathbf{k}}$ being the nabla operator and $|\psi\rangle \equiv |\psi(\mathbf{k})\rangle$ being the \mathbf{k} -dependent Bloch state. We express the Berry connection in curvilinear coordinates

$$\mathbf{A} = i \langle \psi | \partial_{k_r} | \psi \rangle \frac{\hat{\mathbf{e}}_r}{h_r}, \quad (\text{B2})$$

where $h_r = |\mathbf{h}_r|$ is the Lamé factor where $\mathbf{h}_r = (\partial_{k_r} k_v) \hat{\mathbf{e}}_v$ with $v = x, y, z$ running over the Cartesian coordinates and $r = 1, 2, 3$ running over the curvilinear coordinates. Here, $\hat{\mathbf{e}}_v$ is the unit vector in k_v direction and $\hat{\mathbf{e}}_r$ is the unit vector in k_r direction. The Lamé factor is related to the metric tensor as $g_{rs} = \mathbf{h}_r \cdot \mathbf{h}_s$.

Now, we express the curl in curvilinear coordinates

$$\partial_{\mathbf{k}} \times \mathbf{A} = \frac{\epsilon^{rst}}{h_s h_t} (\partial_{k_r} h_s A_s) \hat{\mathbf{e}}_t \quad (\text{B3})$$

$$= \frac{i \epsilon^{rst}}{h_s h_t} (\partial_{k_r} \langle \psi | \partial_{k_s} | \psi \rangle) \hat{\mathbf{e}}_t. \quad (\text{B4})$$

Here, $s, t = 1, 2, 3$. The surface element of the surface spanned by the first and the second coordinate of the curvilinear coordinate system reads as

$$d\mathbf{S} = \mathbf{h}_1 \times \mathbf{h}_2 dk_1 dk_2 \quad (\text{B5})$$

$$= (h_1 \hat{\mathbf{e}}_1) \times (h_2 \hat{\mathbf{e}}_2) dk_1 dk_2 \quad (\text{B6})$$

$$= h_1 h_2 \hat{\mathbf{e}}_1 \times \hat{\mathbf{e}}_2 dk_1 dk_2 \quad (\text{B7})$$

$$= h_1 h_2 \hat{\mathbf{e}}_3 dk_1 dk_2. \quad (\text{B8})$$

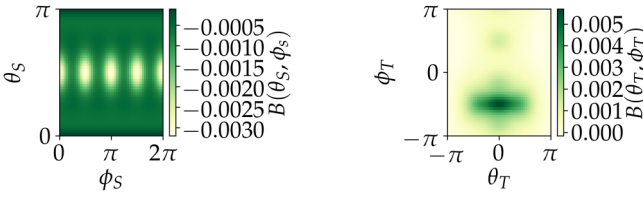


FIG. 14. Berry curvature on the sphere and the torus as a function of the spherical and toroidal angles.

Finally, the Berry curvature element follows as

$$\begin{aligned} d\mathbf{S} \cdot \partial_{\mathbf{k}} \times \mathbf{A} &= h_1 h_2 \hat{\mathbf{e}}_3 \cdot \hat{\mathbf{e}}_1 \frac{i \epsilon^{rst}}{h_r h_s} (\partial_{k_r} \langle \psi | \partial_{k_i} | \psi \rangle) dk_1 dk_2 \\ &= i (\partial_{k_1} \langle \psi | \partial_{k_2} | \psi \rangle - \partial_{k_2} \langle \psi | \partial_{k_1} | \psi \rangle) dk_1 dk_2 \\ &= -2 \text{Im} \langle \partial_{k_1} \psi | \partial_{k_2} \psi \rangle dk_1 dk_2 \end{aligned} \quad (\text{B9})$$

which has the familiar analytical form of the Chern number. Integrating the coordinates k_1 and k_2 within the respective boundaries, the resulting expression directly yields the Chern number without a complicated coordinate transformation.

Examples: Sphere and torus

Let us consider two example curvilinear coordinate system to enclose the WPs: the sphere and the torus. The parametrized surfaces of the sphere $(k_1, k_2) = (\theta_S, \phi_S)$ and the torus $(k_1, k_2) = (\theta_T, \phi_T)$ can be expressed as

$$\begin{pmatrix} k_x(\theta_S, \phi_S) \\ k_y(\theta_S, \phi_S) \\ k_z(\theta_S, \phi_S) \end{pmatrix} = \mathbf{k}_{\text{WP}} + R_S \begin{pmatrix} \sin(\theta_S) \cos(\phi_S) \\ \sin(\theta_S) \sin(\phi_S) \\ \cos(\theta_S) \end{pmatrix} \quad (\text{B10})$$

for the sphere and

$$\begin{pmatrix} k_x(\theta_T, \phi_T) \\ k_y(\theta_T, \phi_T) \\ k_z(\theta_T, \phi_T) \end{pmatrix} = \mathbf{k}_{\text{WP}} + R_T \begin{pmatrix} \cos(\phi_T) \\ \sin(\phi_T) \\ 0 \end{pmatrix} + r_T \begin{pmatrix} \cos(\theta_T) \cos(\phi_T) \\ \cos(\theta_T) \sin(\phi_T) \\ \sin(\theta_T) \end{pmatrix} \quad (\text{B11})$$

for the torus. \mathbf{k}_{WP} denotes the position of the WP in the BZ. The Chern number, or topological charge, then follows by substituting (θ_S, ϕ_S) and (θ_T, ϕ_T) , respectively, for (k_1, k_2) in Eq. (B9). Note that for the torus, the \mathbf{k}_{WP} has to be shifted, e.g., by $R_T \hat{\mathbf{e}}_x$, in order to properly enclose the WP. The results for the Berry curvature as a function of (θ_S, ϕ_S) and (θ_T, ϕ_T) , respectively, are shown in Fig. 14 for the model in Eq. (2). Integrating these Berry curvatures yields 1 and -1 , respectively, according to the two different WPs enclosed. For the sphere, we have used $\mathbf{k}_{\text{WP}} = (0, \pi/2, -\pi/2)$ and $R_S = \pi/2$ and for the torus we have used $\mathbf{k}_{\text{WP}} = (-R_T, \pi/2, \pi/2)$, $R_T = \pi/6$, and $r_T = \pi/6$.

APPENDIX C: SELF-ENERGIES AS DMFT RESULTS

To better understand the correlated nature of our results, we provide the self-energies which were obtained from the DMFT calculations exemplarily for $U = 10$ and 20 . Figure 15 shows the self-energy $\Sigma(i\omega_n)$ as a function of the

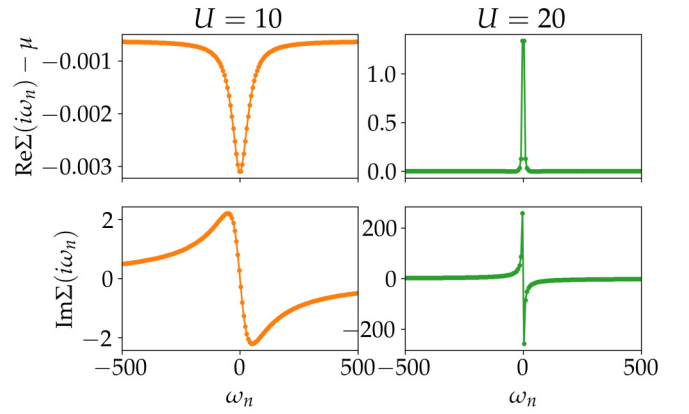


FIG. 15. Self-energy as a function of Matsubara frequencies for $U = 10$ and 20 for $T = 0.1$. We only show the self-energy of one site of the unit cell as it appears that the self-energy of the other site is identical in the present cases.

Matsubara frequencies at $T = 0.1$. In Fig. 16, we present the self-energy after analytical continuation with the Max-Ent method. One can see the symmetry of $\text{Re}\Sigma(-i\omega_n) = \text{Re}\Sigma(i\omega_n)$ and $\text{Im}\Sigma(-\omega) = \text{Im}\Sigma(\omega)$ as well as the antisymmetry of $\text{Im}\Sigma(-i\omega_n) = -\text{Im}\Sigma(i\omega_n)$ and $\text{Re}\Sigma(-\omega) = -\text{Re}\Sigma(\omega)$.

APPENDIX D: REAL VALUEDNESS OF THE ISHIKAWA-MATSUYAMA FORMULA

The invariant in Eq. (15) is purely real. To show this, we reintroduce the frequency argument and define

$$\Lambda_1(i\omega_n) = G(i\omega_n) j_1 G(i\omega_n) j_2 G(i\omega_n) [1 + i\partial_{\omega_n} \Sigma(i\omega_n)], \quad (\text{D1})$$

$$\Lambda_2(i\omega_n) = [1 + i\partial_{\omega_n} \Sigma(i\omega_n)] G(i\omega_n) j_2 G(i\omega_n) j_1 G(i\omega_n) \quad (\text{D2})$$

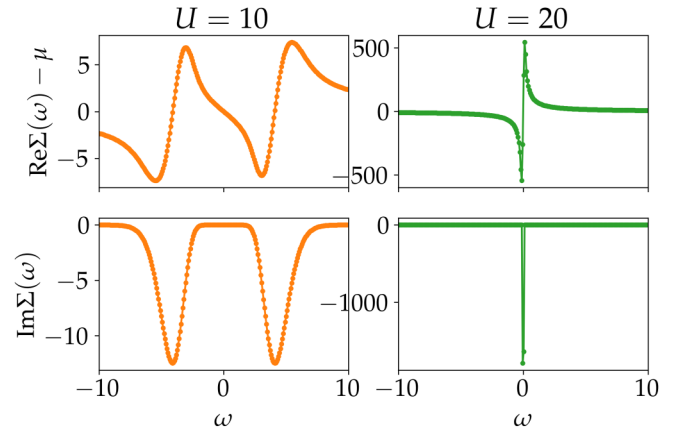


FIG. 16. Self-energy as a function of real frequencies for $U = 10$ and 20 for $T = 0.1$. We only show the self-energy of one site of the unit cell as it appears that the self-energy of the other site is identical in the present cases.

which yields

$$C_{\text{IM}} = \frac{i}{8\pi^2} \int d\mathbf{k} d\omega_n \text{Tr}[\Lambda_1(i\omega_n) - \Lambda_2(i\omega_n)]. \quad (\text{D3})$$

Let us consider the Hermitian conjugate of Λ_1 :

$$[G(i\omega_n)jG(i\omega_n)j_2G(i\omega_n)[1 + i\partial_{\omega_n}\Sigma(i\omega_n)]]^\dagger \quad (\text{D4})$$

$$= [1 + i\partial_{\omega_n}\Sigma(i\omega_n)]^\dagger G^\dagger(i\omega_n)j_2^\dagger G^\dagger(i\omega_n)j_1^\dagger G^\dagger(i\omega_n) \quad (\text{D5})$$

$$= [1 - i\partial_{\omega_n}\Sigma^\dagger(i\omega_n)]G(-i\omega_n)j_2G(-i\omega_n)j_1G(-i\omega_n) \quad (\text{D6})$$

$$= [1 + i\partial_{-\omega_n}\Sigma(-i\omega_n)]G(-i\omega_n)j_2G(-i\omega_n)j_1G(-i\omega_n) \quad (\text{D7})$$

$$= \Lambda_2(-i\omega_n), \quad (\text{D8})$$

where we have used the fact that the currents j_i are Hermitian matrices as well as the symmetries of the Green's function $G^\dagger(i\omega_n) = G(-i\omega_n)$ and the self-energy $\Sigma^*(i\omega_n) = \Sigma(-i\omega_n)$. We thus find that Eq. (D3) can be rewritten as

$$\begin{aligned} C_{\text{IM}} &= \frac{i}{8\pi^2} \int d\mathbf{k} d\omega_n \text{Tr}[\Lambda_1(i\omega_n) - \Lambda_1^\dagger(-i\omega_n)] \\ &= \frac{i}{8\pi^2} \int d\mathbf{k} d\omega_n \text{Tr}[\Lambda_1(i\omega_n) - \Lambda_1^\dagger(i\omega_n)] \\ &= \frac{i}{8\pi^2} \int d\mathbf{k} d\omega_n \sum_l 2i \text{Im}\lambda_l(i\omega_n) \\ &= -\frac{1}{4\pi^2} \int d\mathbf{k} d\omega_n \sum_l \text{Im}\lambda_l(i\omega_n), \end{aligned} \quad (\text{D9})$$

which is purely real. From the first line to the second line, we have used that we integrate over the full frequency range. In the third line we have expressed the trace of $\Lambda_1(i\omega_n)$ in terms of its eigenvalues $\lambda_l(i\omega_n)$.

-
- [1] J. Dalibard, F. Gerbier, G. Juzeliūnas, and P. Öhberg, *Rev. Mod. Phys.* **83**, 1523 (2011).
- [2] N. Goldman, G. Juzeliūnas, P. Öhberg, and I. B. Spielman, *Rep. Prog. Phys.* **77**, 126401 (2014).
- [3] M. Aidelsburger, S. Nascimbene, and N. Goldman, *C. R. Phys.* **19**, 394 (2018).
- [4] W. Hofstetter and T. Qin, *J. Phys. B: At., Mol. Opt. Phys.* **51**, 082001 (2018).
- [5] N. R. Cooper, J. Dalibard, and I. B. Spielman, *Rev. Mod. Phys.* **91**, 015005 (2019).
- [6] I. Bloch, *Nat. Phys.* **1**, 23 (2005).
- [7] I. Bloch, J. Dalibard, and W. Zwerger, *Rev. Mod. Phys.* **80**, 885 (2008).
- [8] D. R. Hofstadter, *Phys. Rev. B* **14**, 2239 (1976).
- [9] F. D. M. Haldane, *Phys. Rev. Lett.* **61**, 2015 (1988).
- [10] M. Aidelsburger, M. Atala, M. Lohse, J. T. Barreiro, B. Paredes, and I. Bloch, *Phys. Rev. Lett.* **111**, 185301 (2013).
- [11] H. Miyake, G. A. Siviloglou, C. J. Kennedy, W. C. Burton, and W. Ketterle, *Phys. Rev. Lett.* **111**, 185302 (2013).
- [12] G. Jotzu, M. Messer, R. Desbuquois, M. Lebrat, T. Uehlinger, D. Greif, and T. Esslinger, *Nature (London)* **515**, 237 (2014).
- [13] N. Fläschner, B. S. Rem, M. Tarnowski, D. Vogel, D.-S. Lühmann, K. Sengstock, and C. Weitenberg, *Science* **352**, 1091 (2016).
- [14] M. Bukov, L. D'Alessio, and A. Polkovnikov, *Adv. Phys.* **64**, 139 (2015).
- [15] A. Eckardt, *Rev. Mod. Phys.* **89**, 011004 (2017).
- [16] S. Ryu, A. P. Schnyder, A. Furusaki, and A. W. W. Ludwig, *New J. Phys.* **12**, 065010 (2010).
- [17] B. Feng, J. Zhang, Q. Zhong, W. Li, S. Li, H. Li, P. Cheng, S. Meng, L. Chen, and K. Wu, *Nat. Chem.* **8**, 563 (2016).
- [18] N. P. Armitage, E. J. Mele, and A. Vishwanath, *Rev. Mod. Phys.* **90**, 015001 (2018).
- [19] S. Rachel, *Rep. Prog. Phys.* **81**, 116501 (2018).
- [20] D. Pesin and L. Balents, *Nat. Phys.* **6**, 376 (2010).
- [21] T. Yoshida, R. Peters, S. Fujimoto, and N. Kawakami, *Phys. Rev. Lett.* **112**, 196404 (2014).
- [22] T. Yoshida and N. Kawakami, *Phys. Rev. B* **94**, 085149 (2016).
- [23] K. Kudo, T. Yoshida, and Y. Hatsugai, *Phys. Rev. Lett.* **123**, 196402 (2019).
- [24] A. Dauphin, M. Müller, and M. A. Martin-Delgado, *Phys. Rev. A* **86**, 053618 (2012).
- [25] A. Dauphin, M. Müller, and M. A. Martin-Delgado, *Phys. Rev. A* **93**, 043611 (2016).
- [26] A. A. Zyuzin, S. Wu, and A. A. Burkov, *Phys. Rev. B* **85**, 165110 (2012).
- [27] S.-Y. Xu, I. Belopolski, N. Alidoust, M. Neupane, G. Bian, C. Zhang, R. Sankar, G. Chang, Z. Yuan, C.-C. Lee, S.-M. Huang, H. Zheng, J. Ma, D. S. Sanchez, B. Wang, A. Bansil, F. Chou, P. P. Shibayev, H. Lin, S. Jia, and M. Z. Hasan, *Science* **349**, 613 (2015).
- [28] L. Lu, Z. Wang, D. Ye, L. Ran, L. Fu, J. D. Joannopoulos, and M. Soljačić, *Science* **349**, 622 (2015).
- [29] C.-L. Zhang, S.-Y. Xu, I. Belopolski, Z. Yuan, Z. Lin, B. Tong, G. Bian, N. Alidoust, C.-C. Lee, S.-M. Huang, T.-R. Chang, G. Chang, C.-H. Hsu, H.-T. Jeng, M. Neupane, D. S. Sanchez, H. Zheng, J. Wang, H. Lin, C. Zhang *et al.*, *Nat. Commun.* **7**, 10735 (2016).
- [30] B. Song, C. He, S. Niu, L. Zhang, Z. Ren, X.-J. Liu, and G.-B. Jo, *Nat. Phys.* **15**, 911 (2019).
- [31] T. Morimoto and N. Nagaosa, *Sci. Rep.* **6**, 19853 (2016).
- [32] M.-F. Yang, *Phys. Rev. B* **100**, 245137 (2019).
- [33] A. Georges, G. Kotliar, W. Krauth, and M. J. Rozenberg, *Rev. Mod. Phys.* **68**, 13 (1996).
- [34] D. Cocks, P. P. Orth, S. Rachel, M. Buchhold, K. Le Hur, and W. Hofstetter, *Phys. Rev. Lett.* **109**, 205303 (2012).
- [35] P. P. Orth, D. Cocks, S. Rachel, M. Buchhold, K. Le Hur, and W. Hofstetter, *J. Phys. B: At., Mol. Opt. Phys.* **46**, 134004 (2013).
- [36] I. Vasić, A. Petrescu, K. Le Hur, and W. Hofstetter, *Phys. Rev. B* **91**, 094502 (2015).
- [37] A. Amaricci, J. C. Budich, M. Capone, B. Trauzettel, and G. Sangiovanni, *Phys. Rev. Lett.* **114**, 185701 (2015).
- [38] T. I. Vanhala, T. Siro, L. Liang, M. Troyer, A. Harju, and P. Törmä, *Phys. Rev. Lett.* **116**, 225305 (2016).

- [39] P. Kumar, T. Mertz, and W. Hofstetter, *Phys. Rev. B* **94**, 115161 (2016).
- [40] A. Amaricci, L. Privitera, F. Petocchi, M. Capone, G. Sangiovanni, and B. Trauzettel, *Phys. Rev. B* **95**, 205120 (2017).
- [41] J.-H. Zheng and W. Hofstetter, *Phys. Rev. B* **97**, 195434 (2018).
- [42] B. Irsigler, J.-H. Zheng, and W. Hofstetter, *Phys. Rev. Lett.* **122**, 010406 (2019).
- [43] B. Irsigler, J.-H. Zheng, M. Hafez-Torbati, and W. Hofstetter, *Phys. Rev. A* **99**, 043628 (2019).
- [44] A. Amaricci, J. C. Budich, M. Capone, B. Trauzettel, and G. Sangiovanni, *Phys. Rev. B* **93**, 235112 (2016).
- [45] B. Irsigler, J.-H. Zheng, F. Grusdt, and W. Hofstetter, *Phys. Rev. Res.* **2**, 013299 (2020).
- [46] L. Crippa, A. Amaricci, N. Wagner, G. Sangiovanni, J. C. Budich, and M. Capone, *Phys. Rev. Res.* **2**, 012023(R) (2020).
- [47] S. Acheche, R. Nourafkan, J. Padayasi, N. Martin, and A.-M. S. Tremblay, *Phys. Rev. B* **102**, 045148 (2020).
- [48] B. Roy, P. Goswami, and V. Juričić, *Phys. Rev. B* **95**, 201102(R) (2017).
- [49] M. Laubach, C. Platt, R. Thomale, T. Neupert, and S. Rachel, *Phys. Rev. B* **94**, 241102(R) (2016).
- [50] T. Dubček, C. J. Kennedy, L. Lu, W. Ketterle, M. Soljačić, and H. Buljan, *Phys. Rev. Lett.* **114**, 225301 (2015).
- [51] T. Fukui, Y. Hatsugai, and H. Suzuki, *J. Phys. Soc. Jpn.* **74**, 1674 (2005).
- [52] E. Gull, A. J. Millis, A. I. Lichtenstein, A. N. Rubtsov, M. Troyer, and P. Werner, *Rev. Mod. Phys.* **83**, 349 (2011).
- [53] M. Caffarel and W. Krauth, *Phys. Rev. Lett.* **72**, 1545 (1994).
- [54] R. W. Helmes, T. A. Costi, and A. Rosch, *Phys. Rev. Lett.* **100**, 056403 (2008).
- [55] M. Snoek, I. Titvinidze, C. Tóke, K. Byczuk, and W. Hofstetter, *New J. Phys.* **10**, 093008 (2008).
- [56] A. I. Lichtenstein, M. G. Zacher, W. Hanke, A. M. Oles, and M. Fleck, *Eur. Phys. J. B* **37**, 439 (2004).
- [57] B. Roy, P. Goswami, and J. D. Sau, *Phys. Rev. B* **94**, 041101(R) (2016).
- [58] Y. Lu, M. Höppner, O. Gunnarsson, and M. W. Haverkort, *Phys. Rev. B* **90**, 085102 (2014).
- [59] M. Jarrell and J. E. Gubernatis, *Phys. Rep.* **269**, 133 (1996).
- [60] K. Ishikawa and T. Matsuyama, *Z. Phys. C* **33**, 41 (1986).
- [61] D. J. Thouless, M. Kohmoto, M. P. Nightingale, and M. den Nijs, *Phys. Rev. Lett.* **49**, 405 (1982).
- [62] Z. Wang and S.-C. Zhang, *Phys. Rev. X* **2**, 031008 (2012).
- [63] J.-H. Zheng, T. Qin, and W. Hofstetter, *Phys. Rev. B* **99**, 125138 (2019).
- [64] T. Yoshida, S. Fujimoto, and N. Kawakami, *Phys. Rev. B* **85**, 125113 (2012).
- [65] J. He, Y.-H. Zong, S.-P. Kou, Y. Liang, and S. Feng, *Phys. Rev. B* **84**, 035127 (2011).
- [66] J. Radić, A. Di. Ciolo, K. Sun, and V. Galitski, *Phys. Rev. Lett.* **109**, 085303 (2012).
- [67] J. Wu, Jean Paul Latyr Faye, D. Sénéchal, and J. Maciejko, *Phys. Rev. B* **93**, 075131 (2016).
- [68] Z.-L. Gu, K. Li, and J.-X. Li, *New J. Phys.* **21**, 073016 (2019).
- [69] M. Ebrahimkhas, M. Hafez-Torbati, and W. Hofstetter, [arXiv:2006.09515](https://arxiv.org/abs/2006.09515).
- [70] V. Gurarie, *Phys. Rev. B* **83**, 085426 (2011).